THE JOURNAL OF PHYSICAL CHEMISTRY C
A JOURNAL OF THE AMERICAN CHEMICAL SOCIETY

pubs.acs.org/JPCC
Article

Insights into the Role of Defects in $Fe_2(MoO_4)_3$ Catalysts

Marcel Dürl, Kevin Sowa, Martin Panthöfer, Niklas Oefner, Danny Stark, Bastian J. M. Etzold, and Angela Möller*

Cite This: J. Phys. Chem. C 2023, 127, 7019−7026

ABSTRACT: The catalytic activity and selectivity of $Fe_2(MoO_4)_3$ obtained from solid-state synthesis protocols is investigated for the oxidative dehydrogenation (ODH) of ethanol to acetaldehyde. While $Fe_2(MoO_4)_3$ annealed in a MoO_3 atmosphere is found to be inactive, ball-milling of such solid-state synthesis precursors leads to an increase in activity, which cannot be attributed purely to the change in the specific surface area nor to a geometric effect of smaller particles. In a systematic study of the synthesis of Fe_2O_3-free $Fe_2(MoO_4)_3$ samples, the correlation of ball-milling time, defect concentration, and catalytic activity is presented. In-depth X-ray diffraction studies, magnetic susceptibility, and ^{57}Fe-Mössbauer spectroscopic measurements disclose characteristic signatures of the defect sites in the solid materials introduced by ball-milling and indicate: (i) MoO_3-enriched amorphous layers of variable thickness (shell-like) and (ii) crystalline bulk defects corresponding to a reduction in the molar volume of the solid. The onset of recrystallization processes sets in around 300 °C and is accompanied by an enhanced MoO_3 mobility in the particles, which adds to an increase in activity and a decreasing selectivity under catalytic conditions. Accordingly, the defects associated with the decreasing amorphous fraction are converted to crystalline bulk defects, which are monitored by the magnetic hyperfine field distribution of the respective Fe sites. Overall, this study shows the importance of the amorphous layer thickness with a sufficient defect concentration and of the bulk defects' contribution to the chemical gradients, important for the MoO_3 mobility and reduction of the MoO_3 loss as a volatile species at the solid/gas phase boundary in ODH catalysis.

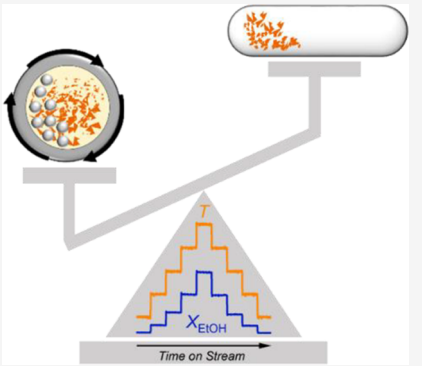

INTRODUCTION

$Fe_2(MoO_4)_3$ belongs to one of the most prominently used transition-metal oxide catalysts for the commercial selective oxidation of methanol to formaldehyde.[1−10] The oxidative dehydrogenation (ODH) of methanol is remarkable as conversion with high selectivity (S) can be achieved in heterogeneous catalysis using $Fe_2(MoO_4)_3$ ($S \geq 92\%$). The established technical catalyst is composed of $Fe_2(MoO_4)_3$ coated with MoO_3. Excess MoO_3 increases the selectivity and the lifetime of the catalyst.[4,5] Additionally, it reduces the amount of volatile MoO_3 originating from the decomposition of $Fe_2(MoO_4)_3$, which would then result in the formation of Fe_2O_3. In principle, MoO_3 accounts for the formation of the aldehyde, while Fe_2O_3 enhances the unwanted total oxidation to CO_2,[3] which underlines the importance of preserving $Fe_2(MoO_4)_3$. Importantly, surface and performance studies[11,12] indicate that additional MoO_3 cannot act as a replenishing reservoir for its loss from $Fe_2(MoO_4)_3$ under catalytic processes on stream below 350 °C. While these dependencies are qualitatively known, structure−property relationships of the $Fe_2(MoO_4)_3$ catalyst in terms of MoO_3 migration to extended surface layers in the solid state and its influence on activity and selectivity are unknown. In order to allow for such a systematic investigation, we focus on a solid-state synthesis route providing pristine $Fe_2(MoO_4)_3$ and variable, extrinsic induced defect concentrations as a result of ball-milling. General details on mechanochemical synthesis routes are given in refs 9 and 13. We explicitly refrain from classical coprecipitation using soluble nitrates or chlorides and sodium molybdate as the sources of less defined or controllable synthesis routes. Employing the aforementioned solid-state protocols enables us to correlate defect concentrations with the sample's history and the physical properties obtained from in-depth X-ray diffraction, ^{57}Fe-Mössbauer spectroscopy, and magnetic measurements. Proof of concept is the catalytic performance of selected $Fe_2(MoO_4)_3$ samples, using the recently demonstrated ethanol ODH protocol.[14]

Received: March 3, 2023
Revised: March 10, 2023
Published: April 4, 2023

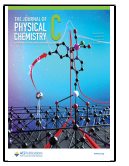

METHODS

Synthesis. $Fe_2(MoO_4)_3$ was synthesized from ground Fe_2O_3 (99.9%, ChemPur) and MoO_3 (99.9%, ChemPur) in a molar ratio of 1:3.1 at 650 °C in evacuated (2×10^{-2} mbar) silica ampules for 200 h in a horizontal tube furnace. The annealing process occurs here in a MoO_3(g) atmosphere. Upon cooling, excess MoO_3(s) separates from $Fe_2(MoO_4)_3$. This pristine sample is referred to as an-$Fe_2(MoO_4)_3$ and taken as the reference. All other $Fe_2(MoO_4)_3$ samples are synthesized via an initial ball-milling (650 rpm, corundum crucibles and nine balls with a diameter of 8−10 mm, t_{bm} = 15 min, Retzsch PM100) of a Fe_2O_3 and MoO_3 mixture (∼16 g) and 10 mL of acetone (≥99.9%, Fischer Chemicals). The mixture was sintered in a corundum crucible under ambient atmosphere at 700 °C for 4.5 h and 850 °C for 0.5 h using a heating rate of 200 °C/h. In the case of an initial molar ratio of 1:3 of Fe_2O_3 and MoO_3, small Fe_2O_3 impurities were present. Therefore, we optimized the ratio to 1:3.04 (based on the amount of hematite originating from the MoO_3 loss under reaction conditions) yielding Fe_2O_3-free bm0-$Fe_2(MoO_4)_3$. In order to further activate (increase of defect concentration) the samples for catalytic processes, each sample was ball-milled again: (i) 6 × 5 min, ac-$Fe_2(MoO_4)_3$ containing ∼3% hematite; (ii) the Fe_2O_3-free bm0-$Fe_2(MoO_4)_3$ sample was consecutively ball-milled in 5 min intervals (6×, samples: bm5, bm10, bm15, bm20, bm25, bm30), twice for an additional 10 min (bm40, bm50), and finally for 25 min (bm75). A small portion of the mixture was kept after each interval and dried for further characterization. This series of compounds from consecutive ball-milling cycles is referenced by bm#-$Fe_2(MoO_4)_3$ with # related to the total ball-milling time (t_{bm}).

Analytical Methods. All samples were characterized by X-ray diffraction performed on a STADI-P diffractometer (STOE&Cie) equipped with Mo−Kα1 radiation (λ = 0.70930 Å), a Ge (111) monochromator, and a MYTHEN 1K detector (Dectris), in transmission geometry from 1.500 to 73.485° in 2Θ (step size 0.015°). Room-temperature data were collected on a flat sample holder using acetate-foil for sample preparation. For in situ high-temperature measurements, a furnace (HT2, STOE&Cie) was used with the sample contained in a capillary under nitrogen or air atmosphere. Each diffraction pattern was recorded after temperature equilibration (heating rate 5 °C/min, in steps of 50 °C up to 250 °C and 15 °C up to 550 °C). All X-ray diffraction data was evaluated by Rietveld methods as implemented in the software package Topas.[15]

Scanning electron microscopy (SEM) investigations were carried out on a Phenom ProX (Phenom-World BV) at an accelerating voltage of 15 kV. EDX analyses were performed with 15 kV accelerating voltage in full BSD mode. Particle sizes were derived and surfaces were calculated: bm0 (l = 12(4) μm, $l_\perp$ = 10(1) μm, area = 130(50) μm^2); bm30 (l = 5.4(9) μm, $l_\perp$ 4.0(9) μm, area = 22(7) μm^2); bm75 (l = 2.6(4) μm, $l_\perp$ 2.2(3) μm, area = 6(1) μm^2). Specific surface areas were determined via argon physisorption analysis at 189.3 °C using a 3Flex analyzer (Micromeritics) after degassing of the samples under vacuum at 200 °C for 18 h. To gain sufficient total surface area for accurate measurements, approximately 1 g of sample was used. Specific surface areas (SSAs) were calculated using the Brunauer−Emmett−Teller (BET) method (3P Instruments) for bm75 (3.46 m^2/g) and ac (2.18 m^2/g), whereas the specific surface area of an-$Fe_2(MoO_4)_3$ was not accessible. Dynamic scanning calorimetry measurements were conducted in Al pans using heating/cooling rates of 20 °C/min and a N_2-gas flow (DSC3+, Mettler-Toledo).

ODH catalytic reactions were carried out in a continuous flow apparatus as described in ref 14. Briefly, 100 mg of the catalyst was placed in a silica-glass tube between two glass wool plugs. Liquid reactants, ethanol ≥99% (Fisher Scientific) were fed to the reactor by using a saturation system and carrier gases Helium 5.0 (Westfalen) and Oxygen 4.8 (liquid air) were dosed by mass flow controllers. The total volume flow was 20 mL/min (STP). Off-gas analytics were performed by an online quadrupole mass spectrometer (GAM 400, InProcess Instruments) and an online gas chromatograph (Shimadzu GC 2010) equipped with an FID and a TCD detector. The gas composition of the reaction products was evaluated by a calibration method using a series of the respective test gas mixtures (O_2, CO, CO_2, C_2H_4). Organic components were determined using a Pt/Al_2O_3 total oxidation catalyst and calibrated via the ratio of excess O_2 to CO_2. For further instrumental details, see ref 16.

Physical Property Measurement. Magnetic measurements were carried out by a physical property measurement system (PPMS, Quantum Design) between 1.8 and 300 K in applied fields of 1000 Oe in field-cooled (fc) and zero-field-cooled (zfc) modes using the VSM option. The samples were pressed to pellets (∼200 mg) with a maximum pressure of 5 bar. A small piece of each pellet (∼10−20 mg) was placed into a plastic capsule and mounted on the brass sample holder for susceptibility measurements.

^{57}Fe Mössbauer Spectroscopy. Mössbauer spectroscopic data was collected in transmission mode on a custom-built instrument setup equipped with a closed-cycle cryostat (C2Montana instruments) using a ^{57}Co(Rh) source in the temperature range from 5 to 300 K. Typically, 25 mg of powdered sample was suspended in ∼100 mg of paraffin (mp 42−44 °C), and the wax-like suspension was spread across a 16 mm diameter PE-disc. The velocity data was calibrated with respect to α-iron foil as an external standard. Spectra were processed using the software package Recoil.[17] Mössbauer spectra between 20 and 250 K were fitted to Voigt lineshapes using the SciPy implementation[18] of the Voigt function and the lmfit module.[19] Fitted parameters for a doublet were signal area (A), chemical shift (CS), quadrupole splitting (QS), and the Voigt line shape parameters (γ and σ). Data handling was achieved using the pandas module.[20] Mössbauer spectra below 12 K were fitted using the xVBF[21] routine implemented in Recoil.[17]

RESULTS AND DISCUSSION

This section is organized as follows: (i) solid-state synthesis aspects and discussion of the formation of $Fe_2(MoO_4)_3$; (ii) ODH catalysis of ethanol comparing annealed (an-), activated (ac-), and ball-milled (bm-) $Fe_2(MoO_4)_3$ materials; (iii) powder X-ray diffraction for the ball-milled series bm#-$Fe_2(MoO_4)_3$ with # referring to the ball-milling time, t_{bm}, in comparison with an-$Fe_2(MoO_4)_3$; (iv) comparison of the magnetic properties; (v) ^{57}Fe Mössbauer spectroscopy used as a local probe for defects.

Synthesis Aspects. $Fe_2(MoO_4)_3$ can be obtained directly from the binary oxide mixtures. However, using stoichiometric amounts of Fe_2O_3 and MoO_3 (1:3 molar ratio) generally results in small impurities of hematite. Responsible for this outcome is that MoO_3 is a volatile reactant at the required high

https://doi.org/10.1021/acs.jpcc.3c01484
J. Phys. Chem. C 2023, 127, 7019−7026

synthesis temperatures ($T_{syn} \geq 650$ °C). Consequently, excess Fe_2O_3 results as an impurity, and we refer to the sample ac-$Fe_2(MoO_4)_3$ here. By using a small surplus of MoO_3 (typical ratio 1:3.04), we observe that Fe_2O_3 impurities can be avoided (bm0-$Fe_2(MoO_4)_3$). The series of ball-milled samples bm#-$Fe_2(MoO_4)_3$ exhibits larger Mo/Fe ratios (up to ~1.8(1)) according to EDX analysis, which indicates enhanced MoO_3 adduct formation near particle surface layers; see further characterization below.

In a second solid-state experiment, we synthesized an-$Fe_2(MoO_4)_3$ from Fe_2O_3 and MoO_3 in a 1:3.1 molar ratio in evacuated silica ampules. We annealed the product at 650 °C for 200 h (equilibration time) in the corresponding saturated MoO_3 atmosphere. Upon cooling in a temperature gradient, excess MoO_3 separates from the product (chemical vapor transport). Such samples, denoted an-$Fe_2(MoO_4)_3$ here, yield a Mo/Fe ratio of 1.50(1) (EDX-analysis) inherent to a pure sample with strongly reduced amounts of extrinsic defects in the bulk; see further characterization below. In Figure 1, we show the SEM photographs of selected samples.

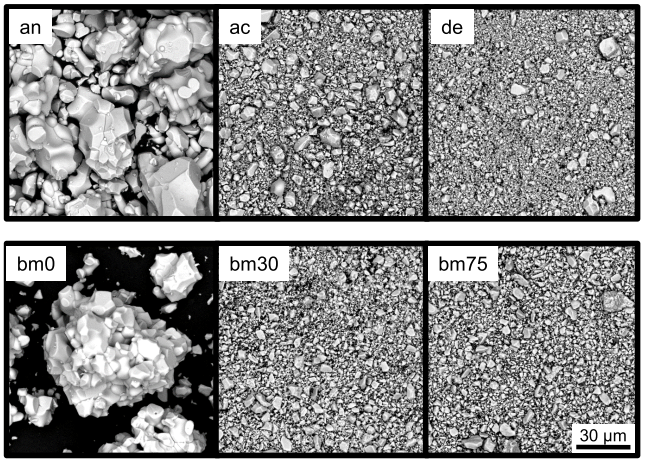

Figure 1. SEM pictures of selected $Fe_2(MoO_4)_3$ samples.

ODH Catalysis. The catalytic activity of an-$Fe_2(MoO_4)_3$, ac-$Fe_2(MoO_4)_3$, and bm75-$Fe_2(MoO_4)_3$ (Figure 1) was investigated for the ODH process of ethanol in a continuous gas flow experiment. The annealed sample (an-$Fe_2(MoO_4)_3$) was treated with the reaction gas mixture for 4 h at 280 °C, resulting in a degree of conversion of less than 5% ethanol to acetaldehyde; see Figure 2. The temperature was stepwise increased to 320 °C within 12 h without enhanced performance. In contrast to the an-$Fe_2(MoO_4)_3$ sample, the activated sample, ac-$Fe_2(MoO_4)_3$, is characterized by a 10% degree of conversion at 200 °C (after an equilibration time on stream of 80 h at 280 °C) and increasing to 52% at 280 °C. This and the high selectivity of acetaldehyde of 96.2% are comparable to a previous study.[14] The spent/deactivated sample (de-$Fe_2(MoO_4)_3$) is further characterized along with the annealed and ball-milled samples of the series; see below.

The activity of bm75-$Fe_2(MoO_4)_3$ was assessed starting from 200 up to 340 °C and afterward again with decreasing temperature to 200 °C. An increase of ethanol conversion up to 84% at 300 °C is observed, underlining the higher activity of the ball-milled sample. However, the selectivity is slightly lower, while diethyl ether is the main side product ($S_{DEE} \approx$

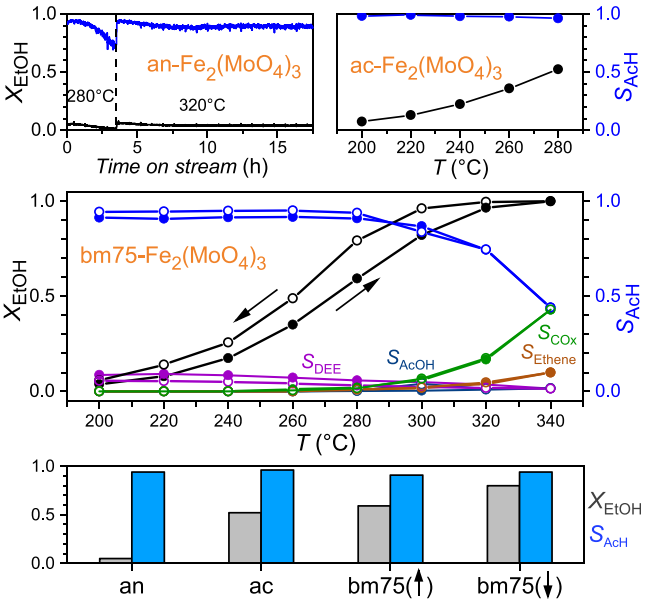

Figure 2. ODH catalysis of an-$Fe_2(MoO_4)_3$ (top, left), temperature-dependence of the catalytic performance of ac-$Fe_2(MoO_4)_3$ (top, right), and bm75-$Fe_2(MoO_4)_3$ (middle). The conversion (X_{EtOH}) and selectivity (S_{AcH}) at 280 °C are shown in the bottom diagram for comparison. Measured with increasing (↑) and decreasing (↓) temperature.

7%). Overall, the initial activity upon heating is comparable with common catalysts obtained from precipitates.[14] Above 300 °C, almost complete ethanol conversion occurs, while CO_x (for simplicity reasons, we give the combined value for separately detected CO and CO_2) and ethene production increase at the expense of acetaldehyde. Structural changes occur around 310 °C (see xrd-data below). Apparently, diffusion processes leading to MoO_3-enriched particle surface layers are involved. Along this line, we interpret the higher activities at 280 °C (X_{EtOH} = 80%, S_{AcH} = 94%) upon cooling as a change in acidity of surface-near regions. Worth mentioning is that the bm75-$Fe_2(MoO_4)_3$ sample upon cooling on stream is almost as active as a MoO_3-coated $Fe_2(MoO_4)_3$ precipitation catalyst.[16] The only difference is that the former requires slightly higher temperatures. It should be emphasized that coking is not observed, as confirmed by the monitored carbon balance during the experiment.

X-ray Diffraction. Rietveld refinements of X-ray diffraction data at room temperature were carried out for all samples and confirm the crystal structure of the low-temperature polymorph (space group $P2_1/a$, Z = 8); see Table 1. Upon increasing ball-milling time (t_{bm}), shear strain is induced, which mainly causes molybdate units to split, whereby direct Fe-O-Fe bonds and weakly bound MoO_3 are formed. The latter becomes increasingly mobile with increasing temperature (e.g., duration of ball-milling time) and diffuses into amorphous surface layers, leading to slightly increasing Mo/Fe ratios of ~1.8 according to our EDX analysis. Concomitantly, the cell volume of the crystalline bulk (core particle) shrinks by ~0.2%. Cell volumes for the differently prepared $Fe_2(MoO_4)_3$ samples are given in Table 1 and corroborate this scenario; compare also an- with bm#-$Fe_2(MoO_4)_3$ with $\Delta V_m \approx -2$ Å^{-3} (Figure 3).

In Figure 3(a), we show diffraction data at room temperature for the ball-milled series (bm#-$Fe_2(MoO_4)_3$)

https://doi.org/10.1021/acs.jpcc.3c01484
J. Phys. Chem. C 2023, 127, 7019−7026

Table 1. Lattice Constants and Cell Volumes for $Fe_2(MoO_4)_3$ ($P2_1/a$) at Room Temperature[a]

	a (Å)	b (Å)	c (Å)	β (deg.)	V (Å^3)
an-	15.6991(1)	9.23684(9)	18.2260(2)	125.2294(9)	2158.92(9)
ac-	15.6938(2)	9.2346(1)	18.2256(9)	125.2256(9)	2156.93(5)
de-	15.6817(1)	9.2278(9)	18.2070(2)	125.2200(9)	2152.40(5)
bm#-	15.689(2)	9.232(6)	18.214(2)	125.222(3)	2155.0(5)
HT-bm75-	15.6863(3)	9.2299(1)	18.2103(3)	125.226(1)	2153.75(7)
ref 25	15.737(8)	9.231(5)	18.224(9)	125.46(2)	2156(4)
ref 26	15.693(3)	9.235(1)	18.218(4)	125.21(1)	2157.2

[a]For the ball-milled series (bm#), the averaged values are given. The sample bm75-$Fe_2(MoO_4)_3$ after heat treatment at 450 °C is given for comparison (HT-bm75).

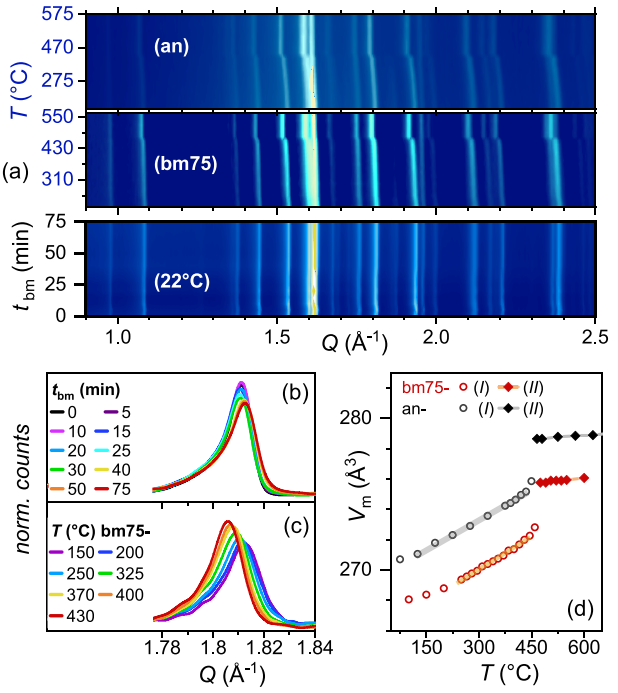

Figure 3. (a) Contour plots: temperature-dependence of an- and bm75-$Fe_2(MoO_4)_3$ and as a function of t_{bm} for the bm#-$Fe_2(MoO_4)_3$ series. (b) Ball-milling time-dependence of the reflection at $Q \approx 1.81$ Å^{-1} for the bm#-$Fe_2(MoO_4)_3$ series at 22 °C. (c) Temperature-dependence of the reflection at $Q \approx 1.81$ Å^{-1} for the bm75-$Fe_2(MoO_4)_3$ sample. (d) Temperature-dependence of the molar volume for bm75-$Fe_2(MoO_4)_3$ and an-$Fe_2(MoO_4)_3$.

with increasing cycling time, t_{bm}. Overall, the broadening of reflections (coherent scattering volume) is moderate and well in line with a homogeneous microcrystalline sample (see particle size distribution in Figure 1 and details given in the experimental section). However, noticeable is the gradual shift to slightly larger Q-values for increasing $t_{bm} \geq 30$ min. This corresponds to a decrease in cell volume upon increasing the duration of a single ball-milling cycle from 5 to 10 or 25 min (Table 1). Interestingly, the cell volumes at 22 °C decrease not only with t_{bm} but even further after annealing (HT-bm75-) or after catalytic processing (de-); see Table 1. This corroborates the mobility of the MoO_3 in a particle due to a chemical gradient. Additional loss of this volatile species at higher temperatures or on stream under catalytic reaction (non-equilibrium) further enhances the MoO_3 mobility in the solid state. In Figure 3(b), the reflection around 1.81 Å^{-1} serves as an example for the decreasing lattice constants and the increasing ratio of amorphous/microcrystalline to crystalline/bulk phase fractions as seen from the shift and the decreasing intensity.

In an in situ experiment, we studied the temperature-dependence of the bm75-$Fe_2(MoO_4)_3$ sample (Figure 3(a,c)). Since the ODH catalysis of ethanol is an exothermic process ($\Delta H° = -172.35$ kJ/mol[22]), it is clear that so-called hot spots induce a sintering process by which the amount of local defect centers in the solid is reduced. In order to probe for such an effect (without the fraction of oxygen mobility due to the chemical gradient of the reoxidation process under catalytic operation), we investigated bm75-$Fe_2(MoO_4)_3$ with increasing temperature. Noticeable is the enhancement of the Bragg reflection intensity upon heating, which can be associated with the increasing crystallinity of the sample. Such a recrystallization process sets in around 300 °C, which is the onset of decreasing selectivity in the ODH process; see Figure 2. In this temperature range, the lattice constants start to increase with similar expansion coefficients as the reference sample an-$Fe_2(MoO_4)_3$; see Figure 3(d) and Table 2. It should be noted

Table 2. Thermal Expansion Coefficients α_i in Units of 10^{-6} K^{-1} for an-$Fe_2(MoO_4)_3$ and bm75-$Fe_2(MoO_4)_3$[a]

	α_a	α_b	α_c	α_β	α_V
(I)an-	16(1)	16(1)	21(1)	2(1)	48(1)
(II)an-	7(1)	1(1)	−2(1)	-	6(1)
(I)bm75-	17(1)	16(1)	21(1)	3(1)	46(2)
(II)bm75-	6(1)	1(1)	−2(1)	-	8(2)

[a]The transition from the monclinic (I) to the orthorhombic (II) polymorph occurs around 470°C.

that the onset temperature of the linear thermal expansion is shifted by almost 150 °C for the bm75-sample in comparison with the annealed one. We suggest that the increasing thermal expansion allows for an enhanced MoO_3 mobility, which results in the enrichment of MoO_3 in the amorphous (shell-like) surface layers as indicated by the ODH catalysis by increasing activity; see Figure 2.

Both an- and bm75-$Fe_2(MoO_4)_3$ exhibit very similar linear thermal expansion coefficients in the two polymorphs, below ~470 °C (I, $P2_1/a$) and above the structural transition to the orthorhombic phase (II, $Pbcn$); see Table 2 and Figure 3(d). This observation is in agreement with the reported ferroelastic transition (499 °C from DSC measurements[23]) and a diffraction study[24] revealing the presence of the high-temperature polymorph at 472 °C. Our DSC measurements indicate that the enthalpy of the phase transition is reduced for the ball-milled compounds as well as for the sintered HT-bm75-sample in comparison with an-$Fe_2(MoO_4)_3$. This

https://doi.org/10.1021/acs.jpcc.3c01484
J. Phys. Chem. C 2023, 127, 7019−7026

implies a smaller fraction of crystalline phase in the former and points toward the existence of amorphous surface coatings. One might infer from this observation that the disordered structure of the latter is possibly more closely related to the high-temperature polymorph of $Fe_2(MoO_4)_3$ (II).

Magnetic Properties. In Figure 4, we present the temperature-dependent reciprocal magnetic susceptibility for

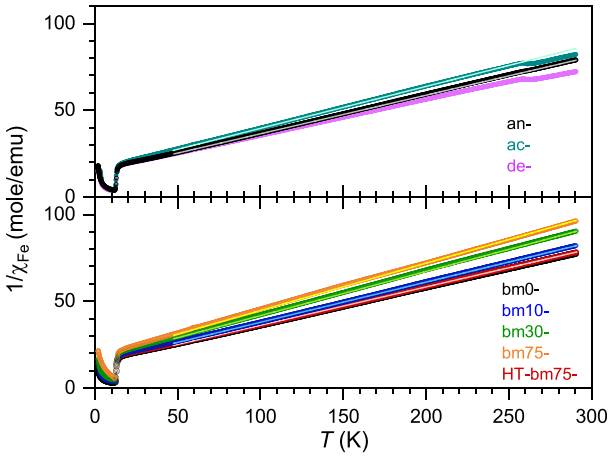

Figure 4. Reciprocal magnetic susceptibility measured in zero-field mode in an applied magnetic field of 1000 Oe for $Fe_2(MoO_4)_3$ samples used for catalysis (top) and representative for the ball-milling series (bottom). Light colored lines denote fits to the respective data.

selected samples. We compare all data to an-$Fe_2(MoO_4)_3$, which we take as a reference. First, we comment on the high-temperature range, where the data can be fitted to a Curie–Weiss law. For an-$Fe_2(MoO_4)_3$, we obtain C = 4.40 K·emu/mol, well in line with the spin-only value of 4.377 K·emu/mol. The derived Weiss constant, $\Theta = -64$ K, corresponds to the value reported in the literature.[27] The ac-$Fe_2(MoO_4)_3$ sample has been subjected to ball-milling as an activation step prior to ODH catalysis and contains small amounts of Fe_2O_3 (hematite); see below. We observe a kink around 250 K that corresponds to the antiferromagnetic *Morin*-transition of α-Fe_2O_3.[28] In the temperature range above 12 K, the deviation in slope from an-$Fe_2(MoO_4)_3$ can be accounted for by a diamagnetic fraction (MoO_3) and a hematite impurity. After the catalytic process, de-$Fe_2(MoO_4)_3$ exhibits lower $\chi^{-1}(T)$ values, which are attributed to decreasing amounts of the volatile MoO_3 (e.g., spent and lost during the catalysis). However, the amount of hematite remains almost constant (see below), as it arises purely from sintering in the solid-state synthesis of equimolar ratios of the binary oxides prior to the activation by ball-milling.

Next, we focus on the ball-milled series bm#-$Fe_2(MoO_4)_3$ containing no Fe_2O_3 as an impurity. With increasing t_{bm}, the slope of $\chi^{-1}(T)$ changes. Thus, an additional diamagnetic contribution (MoO_3) to the magnetic $Fe_2(MoO_4)_3$ (including Fe^{III} defects) becomes evident. We fitted the data for the bm-series to a modified Curie–Weiss law, accounting for bound Fe^{III} defects by an effective constant C* = 4.55 K·emu/mol and kept $\Theta = -64$ K as a constant. Here, χ_0 refers to the diamagnetic value of MoO_3 (-8×10^{-5} emu/mol) and $A + B = 1$ (eq 1).

$$\chi = A \cdot \frac{C^*}{T - \Theta} + B \cdot \chi_0 \tag{1}$$

The diamagnetic contribution represented by the coefficient B increases from 0 (bm0-) to 0.2 (bm75-). It implies that amorphous surface layers of variable thickness (difference in volume fractions) are created by ball-milling, which contain a surplus of MoO_3 in agreement with observations from EDX, X-ray diffraction experiments, and the enhanced catalytic performance. Interestingly, sintering almost reverses the process, and HT-bm75-$Fe_2(MoO_4)_3$ exhibits similar magnetic properties as the starting material bm0-$Fe_2(MoO_4)_3$, again supporting the MoO_3 mobility in a particle at elevated temperatures. For insights into the Fe-site associated defects, we refer to the local probe of Mössbauer spectroscopy below.

Finally, we note that the onset temperature of long-range magnetic order around 12 K is observed for all samples and in line with the literature.[27,29,30] However, at $T \leq 12$ K, the temperature-dependence suggests a dissimilar evolution of the ordered phase for the studied samples. We will comment on this aspect below.

^{57}Fe Mössbauer Spectroscopy. Mössbauer spectroscopic data were recorded from 5 to 250 K. In the paramagnetic regime, we find similar hyperfine parameters (chemical shift, CS, and quadrupole splitting, QS) for all samples. We fitted the spectra by applying a Voigt model (eq 2) to extract further information on line broadening with increasing t_{bm}.

$$V(x, \sigma, \gamma) = \int G(x', \sigma) L(x - x', \gamma) dx' \tag{2}$$

Here, the distribution parameter σ refers to the particle homogeneity. The stress or strain resulting from dislocation or shear-plane defects corresponds to a spectral line broadening equivalent to pressure effects and is represented by the parameter γ.

In Figure 5 (left), we show the Mössbauer spectra of bm75-$Fe_2(MoO_4)_3$ and an-$Fe_2(MoO_4)_3$ at 200 K to illustrate the difference in line shapes of ball-milled and activated samples vs sintered, annealed, or spent/deactivated ones. On the right of Figure 5, the fit parameters to eq 2 are given. The temperature-dependence of CS and QS is representative for all studied

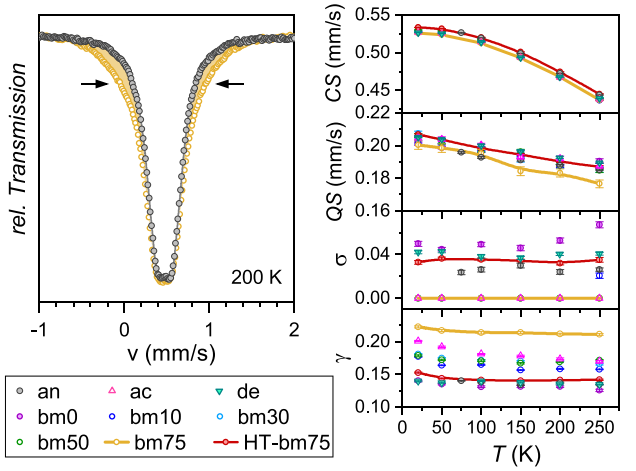

Figure 5. (Left) Mössbauer spectra for bm75- and an-$Fe_2(MoO_4)_3$ at 200 K showing asymmetric line broadening. (Right) $Fe_2(MoO_4)_3$ sample parameter obtained from Voigt fits (eq 2). As a guide to the eye, lines are inserted for bm75- (yellow) and HT-bm75- (red).

https://doi.org/10.1021/acs.jpcc.3c01484
J. Phys. Chem. C 2023, 127, 7019−7026

samples, indicative of Fe^{III} with a relative small anisotropy of the electric field gradient and in good agreement with refs 27 and 29. We notice that the respective CS and QS values slightly decrease with t_{bm} for a given temperature. For the annealed samples (an-, bm0-, HT-bm75, and de-$Fe_2(MoO_4)_3$), the σ-parameter is largest throughout, while all ball-milled samples are represented by $\sigma \approx 0$. Contrarily, the γ-values for ball-milled samples increase with t_{bm}. We interpret the γ parameter as representative of defects in the increasing fraction of amorphous surface layers through ball-milling. This is well in line with the observation of anomalous broadening with heating as reported for the high-temperature $Fe_2(MoO_4)_3$ polymorph.[31] All annealed samples are represented by $\gamma \approx 0.14$, which relates to a material constant. Hence, the degree of particle homogenity and stress of a given sample becomes measurable.

The ferrimagnetic long-range magnetic order (LRO) sets in below 12 K for all studied samples. In Figure 6 (left), we show

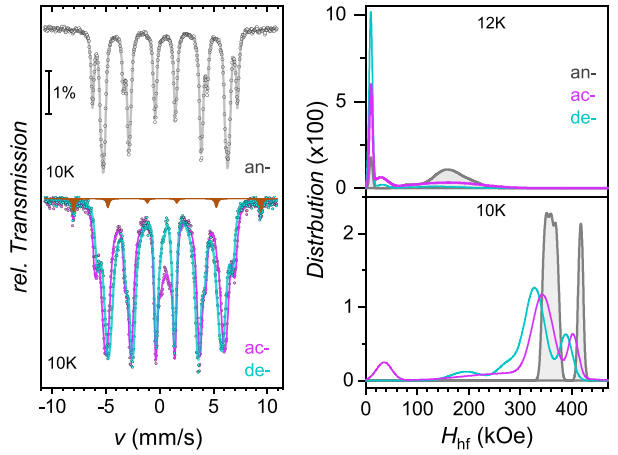

Figure 6. (Left) Mössbauer spectroscopic data (cirles) of an-, ac-, and de-$Fe_2(MoO_4)_3$ at 10 K. The brown-shaded area refers to the α-Fe_2O_3 impurity. (Right) Distribution of hyperfine magnetic fields for $T \leq T_{LRO} \approx 12$ K.

magnetic Mössbauer spectra for the an-, ac-, and de-$Fe_2(MoO_4)_3$ samples. The spectrum for an-$Fe_2(MoO_4)_3$ can be fitted by a Lorentzian line-width analysis constituting of four sextets of equally weighted Fe sites, three with very similar hyperfine field parameters (H_{hf}) and one clearly distinguishable, Table 3. These four subspectra are sextets with the ideal

Table 3. Hyperfine Parameters for an-$Fe_2(MoO_4)_3$ at 10 K

Sites	CS (mm/s)	ϵ (mm/s)	H_{hf} (kOe)	w (mm/s)
Fe1	0.53(1)	−0.02(2)	417.6(2)	0.158(3)
Fe2	0.53(1)	−0.00(3)	370.9(2)	0.157(4)
Fe3	0.53(1)	0.01(2)	358.6(3)	0.144(4)
Fe4	0.53(1)	−0.02(2)	347.1(3)	0.164(4)

3:2:1:1:2:3 intensity ratios expected for static magnetic order. In contrast, the Mössbauer data for ac- and de-$Fe_2(MoO_4)_3$ are distinctly different, as these consist of spectral weight around 0.53 mm/s (CS) and additional contributions to the four inner sextet lines. This means that a measurable percentage of Fe sites is still in the fluctuating state with a distribution of magnetic hyperfine fields experienced by the iron nuclei. In order to fit these data and gain insights into the obvious defect associated spectral weight, we fitted the spectra using the Voigt function based xVBF-routine implemented in the Recoil software.[17,21] Furthermore, as has been pointed out above, the ac- and de-$Fe_2(MoO_4)_3$ samples contain a hematite impurity of ∼3 at-%.

In Figure 6 (right), we show the distribution of H_{hf} obtained from xVBF analysis for the an-, ac-, and de-$Fe_2(MoO_4)_3$ samples. At $T \leq 12$ K $\approx T_{LRO}$, strong fluctuations (nearly paramagnetic) dominate with $H_{hf} \approx 10$ kOe. A broad feature associated with the transition into the long-range ordered state is observed around 150 kOe, clearly smeared out for the ac- and de-samples. An additional, intriguing feature is located around 40 kOe and only present in the activated (ball-milled) samples. We take this feature as a fingerprint of defects linked to the ball-milling induced activation of the catalyst, as it remains observable down to lower temperatures.

At 10 K, the static magnetic LRO is established for the annealed sample indicated by the four narrow equally strong contributions to $P(H_{hf})$; see Table 3. The distribution functions for the ac- and de-samples reveal broadening and a tail at lower hyperfine fields. These serve as an indicator of bulk defects reminiscent of dislocation and nonstoichiometry (Figure 6). Interestingly, the two maxima representing the LRO state (∼300 and 450 kOe) are shifted differently, with the lowest values obtained for the deactivated/spent sample after catalysis. This implies that defects in amorphous surface layers, representative for activated $Fe_2(MoO_4)_3$ samples ($H_{hf} \approx 40$ kOe, ac-$Fe_2(MoO_4)_3$), are shifted to crystalline bulk environments. Thereby, the fraction with $H_{hf} \approx 150$ kOe (de-$Fe_2(MoO_4)_3$) increases. Such degradation effects stemming from the ODH process, along with sintering due to hot spots, eliminate the activated sites ($H_{hf} \approx 40$ kOe) present in ac-$Fe_2(MoO_4)_3$.

Next, we compare the samples of the ball-milled series, bm#-$Fe_2(MoO_4)_3$; see Figure 7. The $\chi(T)$ data confirm the same T_{LRO} but approach the long-range ordered state differently, namely reduced ferrimagnetic exchange with increasing t_{bm}. Despite the similar $\chi^{-1}(T)$ behavior of bm0- and HT-bm75-$Fe_2(MoO_4)_3$ at high temperatures (Figure 4), these two samples differ below T_{LRO}. The annealing time and high temperatures mainly healed those defects that are associated with the activation of the catalyst (MoO_3-enriched amorphous surface layers) and thus place HT-bm75-$Fe_2(MoO_4)_3$ close to the dominating bulk properties of bm10-$Fe_2(MoO_4)_3$; compare also the distribution functions of these two given in Figure 7 (right). Overall, the bm75-sample exhibits the lowest $\chi(T)$-values below T_{LRO}, which underlines the reduced crystalline bulk fraction with a larger defect concentration.

The Mössbauer spectra and xVBF fits to the data for bm75-$Fe_2(MoO_4)_3$ are displayed in Figure 7 (left, bottom) and show an increase in spectral contribution around 0.53 mm/s; compare also with the spectra of ac-$Fe_2(MoO_4)_3$ and recall the absence of this feature for an-$Fe_2(MoO_4)_3$ (Figure 6). The strongly enhanced contribution of those Fe sites with $H_{hf} \approx 40$ kOe (spectral weight around 0.53 mm/s) is a fingerprint for the precatalytic activation of $Fe_2(MoO_4)_3$ by ball-milling and hence largest for bm75-$Fe_2(MoO_4)_3$. We emphasize that this sample indeed exhibits the highest degree of conversion in the ODH of ethanol; see Figure 2.

Additionally, the defect sites associated with the broad feature around $H_{hf} \approx 150$ kOe do not vanish completely for bm75-$Fe_2(MoO_4)_3$, whereas for all other samples, these are

https://doi.org/10.1021/acs.jpcc.3c01484
J. Phys. Chem. C 2023, 127, 7019−7026

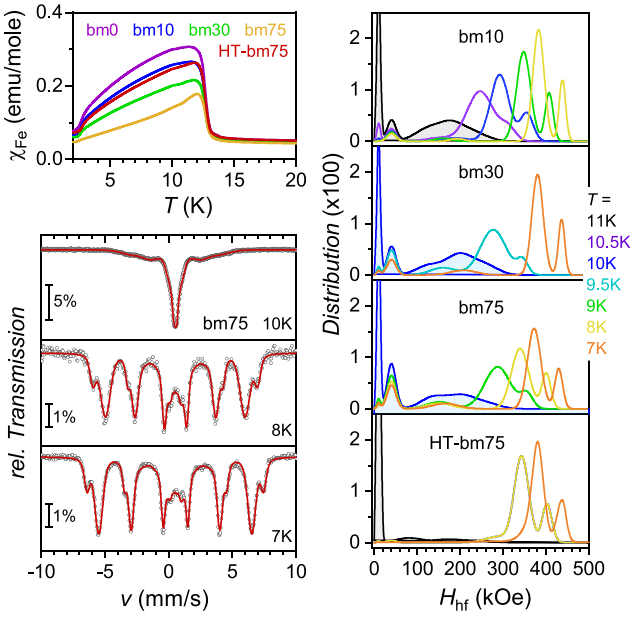

Figure 7. (Left, top) Temperature-dependent susceptibility for bm0-, bm10-, bm30-, bm75-, and HT-bm75-$Fe_2(MoO_4)_3$ below T_{LRO}. (Left, bottom) Mössbauer spectroscopic data (cirles) for bm75-$Fe_2(MoO_4)_3$ at selected temperatures (circles: experiment, red lines: fit). (Right) Distribution of hyperfine magnetic fields at selected temperatures ($T \leq T_{LRO}$) for bm10-, bm30-, bm75-, and HT-bm75-$Fe_2(MoO_4)_3$.

drastically reduced toward lower temperatures and almost vanish for annealed or sintered samples. Hence, we take this feature as the cause of differences in $\chi(2\,K)$ and attribute this to the signature of defects in the crystalline bulk.

CONCLUSIONS

Well-defined samples of $Fe_2(MoO_4)_3$ prepared by solid-state synthesis and further subjected to ball-milling are investigated. We demonstrate the strong activity increase with ball-milling time for the ODH of ethanol. Particle sizes with a surface area of ~3.46 m^2/g exhibit catalytic performance similar to MoO_3-coated $Fe_2(MoO_4)_3$. While the increase in specific surface area is only a minor contribution to the activity increase, structural aspects are more important. X-ray diffraction experiments of such ball-milled samples indicate that defects effectively reduce the molar volume in the coherent scattering volume (lower crystallinity). From EDX analysis, microcrystalline bulk materials with amorphous, MoO_3-enriched surface layers with variable thickness (volume) are established. The thickness of the shell-like amorphous volume fraction increases with ball-milling time. The catalytic active component, MoO_3, increases the performance of a catalyst for the ODH process of ethanol to acetaldehyde. Magnetization and ^{57}Fe Mössbauer spectroscopic investigations reveal two type of defects. This is in line with an increasing amount of the diamagnetic volume fraction (MoO_3) in surface layers of variable thickness. In the magnetically long-range ordered phase, fingerprints of Fe sites associated with the principal defects in bulk and surface layers can be classified by hyperfine magnetic fields of ($H_{hf} \approx$ 150 kOe) and ($H_{hf} \approx$ 40 kOe). These defect-related features are shown to vanish after catalytic processing or upon prolonged sintering. However, in ball-milled samples, the nonstoichiometry of the crystalline bulk $Fe_2(MoO_4)_3$ remains, as indicated by the larger hyperfine-field distribution and strain (γ parameter, see eq 2) compared to stoichiometric an-$Fe_2(MoO_4)_3$. It is speculated that especially the bulk defects are important to provide good MoO_3 transfer to the terminating surface layers. Concomitantly, a continuous surface regeneration of the catalyst is established. Furthermore, thick amorphous surface layers prevent contact of the reaction gas with underlying MoO_3-depleted (bulk) Fe-O centers, which would lead to lower selectivities. According to our Mössbauer studies, we can exclude the presence of hematite in all ball-milled samples (variation in bulk to surface layer fractions) and in the stoichiometric, all-crystalline bulk represented by an-$Fe_2(MoO_4)_3$.

AUTHOR INFORMATION

Corresponding Author

Angela Möller − *Department of Chemistry, Johannes Gutenberg-University, 55128 Mainz, Germany;* orcid.org/0000-0002-3323-6998; Email: angela.moeller@uni-mainz.de

Authors

Marcel Dürl − *Department of Chemistry, Johannes Gutenberg-University, 55128 Mainz, Germany*

Kevin Sowa − *Department of Chemistry, Johannes Gutenberg-University, 55128 Mainz, Germany*

Martin Panthöfer − *Department of Chemistry, Johannes Gutenberg-University, 55128 Mainz, Germany*

Niklas Oefner − *Ernst-Berl-Institut für Makromolekulare und Technische Chemie, Technische Universität Darmstadt, 64287 Darmstadt, Germany*

Danny Stark − *Ernst-Berl-Institut für Makromolekulare und Technische Chemie, Technische Universität Darmstadt, 64287 Darmstadt, Germany*

Bastian J. M. Etzold − *Ernst-Berl-Institut für Makromolekulare und Technische Chemie, Technische Universität Darmstadt, 64287 Darmstadt, Germany;* orcid.org/0000-0001-6530-4978

Complete contact information is available at: https://pubs.acs.org/10.1021/acs.jpcc.3c01484

Notes

The authors declare no competing financial interest.

ACKNOWLEDGMENTS

Funded by the Deutsche Forschungsgemeinschaft (DFG, German Research Foundation) Project-IDs: 442589410 and 443703006, CRC 1487.

REFERENCES

(1) Soares, A.; Farinha Portela, M.; Kiennemann, A.; Hilaire, L.; Millet, J. Iron molybdate catalysts for methanol to formaldehyde oxidation: effects of Mo excess on catalytic behaviour. *Appl. Catal. A* **2001**, *206*, 221−229.

(2) Soares, A. P. V.; Portela, M. F.; Kiennemann, A. Methanol Selective Oxidation to Formaldehyde over Iron-Molybdate Catalysts. *Catal. Rev.* **2005**, *47*, 125−174.

(3) Bowker, M.; Holroyd, R.; House, M.; Bracey, R.; Bamroongwongdee, C.; Shannon, M.; Carley, A. The Selective Oxidation of Methanol on Iron Molybdate Catalysts. *Top. Catal.* **2008**, *48*, 158−165.

(4) House, M. P.; Shannon, M. D.; Bowker, M. Surface segregation in iron molybdate catalysts. *Catal. Lett.* **2008**, *122*, 210−213.

https://doi.org/10.1021/acs.jpcc.3c01484
J. Phys. Chem. C 2023, 127, 7019−7026

(5) Söderhjelm, E.; House, M. P.; Cruise, N.; Holmberg, J.; Bowker, M.; Bovin, J.-O.; Andersson, A. On the Synergy Effect in MoO_3-$Fe_2(MoO_4)_3$ Catalysts for Methanol Oxidation to Formaldehyde. *Top. Catal.* **2008**, *50*, 145.
(6) Ivanov, K. I.; Dimitrov, D. Y. Deactivation of an industrial iron-molybdate catalyst for methanol oxidation. *Catal. Today* **2010**, *154*, 250−255.
(7) Brookes, C.; Wells, P. P.; Dimitratos, N.; Jones, W.; Gibson, E. K.; Morgan, D. J.; Cibin, G.; Nicklin, C.; Mora-Fonz, D.; Scanlon, D. O.; et al. The Nature of the Molybdenum Surface in Iron Molybdate. The Active Phase in Selective Methanol Oxidation. *J. Phys. Chem. C* **2014**, *118*, 26155−26161.
(8) Raun, K. V.; Lundegaard, L. F.; Chevallier, J.; Beato, P.; Appel, C. C.; Nielsen, K.; Thorhauge, M.; Jensen, A. D.; Høj, M. Deactivation behavior of an iron-molybdate catalyst during selective oxidation of methanol to formaldehyde. *Catal. Sci. Technol.* **2018**, *8*, 4626−4637.
(9) Liu, X.; Kong, L.-t.; Liu, C.-f.; Xu, S.-t.; Zhang, D.-d.; Ma, F.-y.; Lu, Z.-p.; Sun, J.-g.; Chen, J. Study on the formation process of $MoO_3/Fe_2(MoO_4)_3$ by mechanochemical synthesis and their catalytic performance in methanol to formaldehyde. *J. Therm. Anal. Calorim.* **2020**, *142*, 1363−1376.
(10) Malik, M. I.; Abatzoglou, N.; Achouri, I. E. Methanol to Formaldehyde: An Overview of Surface Studies and Performance of an Iron Molybdate Catalyst. *Catalysts* **2021**, *11*, 893.
(11) Gaur, A.; Schumann, M.; Raun, K. V.; Stehle, M.; Beato, P.; Jensen, A. D.; Grunwaldt, J.-D.; Høj, M. Operando XAS/XRD and Raman Spectroscopic Study of Structural Changes of the Iron Molybdate Catalyst during Selective Oxidation of Methanol. *ChemCatChem.* **2019**, *11*, 4871−4883.
(12) Raun, K. V.; Lundegaard, L. F.; Beato, P.; Appel, C. C.; Nielsen, K.; Thorhauge, M.; Schumann, M.; Jensen, A. D.; Grunwaldt, J.-D.; Høj, M. Stability of Iron-Molybdate catalysts for selective oxidation of methanol to formaldehyde: Influence of preparation method. *Catal. Lett.* **2020**, *150*, 1434−1444.
(13) Amrute, A. P.; De Bellis, J.; Felderhoff, M.; Schüth, F. Mechanochemical Synthesis of Catalytic Materials. *Chem. Eur. J.* **2021**, *27*, 6819−6847.
(14) Oefner, N.; Heck, F.; Dürl, M.; Schumacher, L.; Khatoon Siddiqui, H.; Kramm, U. I.; Hess, C.; Möller, A.; Albert, B.; Etzold, B. J. M. Activity, Selectivity and Initial Degradation of Iron Molybdate in the Oxidative Dehydrogenation of Ethanol. *ChemCatChem.* **2022**, *14*, No. e202101219.
(15) Coelho, A. A. *TOPAS-Academic V7*. 2020; http://www.topas-academic.net/.
(16) Stark, D. Heterogen katalysierte Gasphasenoxidation einfacher Alkohole an Eisenmolybdaten. Master Thesis, TU Darmstadt, 2022.
(17) Lagarec, K.; Rancourt, D. R. *Recoil - Mössbauer spectral analysis software for Windows*; Department of Physics, University of Ottawa, 1998.
(18) Virtanen, P.; Gommers, R.; Oliphant, T. E.; Haberland, M.; Reddy, T.; Cournapeau, D.; Burovski, E.; Peterson, P.; Weckesser, W.; Bright, J.; et al. SciPy 1.0: Fundamental Algorithms for Scientific Computing in Python. *Nat. Methods* **2020**, *17*, 261−272.
(19) Newville, M.; Otten, R.; Nelson, A.; Ingargiola, A.; Stensitzki, T.; Allan, D.; Fox, A.; Carter, F.; Michał; Osborn, R.; et al. *lmfit/lmfit-py: 1.0.3*, 2021. DOI: 10.5281/zenodo.5570790.
(20) Reback, J.; jbrockmendel; McKinney, W.; den Bossche, J. V.; Augspurger, T.; Roeschke, M.; Hawkins, S.; Cloud, P.; gfyoung; Sinhrks. *pandas-dev/pandas: Pandas 1.4.2*, 2022. DOI: 10.5281/zenodo.6408044
(21) Lagarec, K.; Rancourt, D. R. Extended Voigt-Based Analytic Lineshape Method for Determining N-Dimensional Correlated Hyperfine Parameter Distributions in Mössbauer Spectroscopy. *Nucl. Instrum. Methods Phys. Res. B* **1997**, *129*, 266−280.
(22) Heintz, A. *Thermodynamik der Mischungen*, 1st ed.; Springer Spektrum, 2017. DOI: 10.1007/978-3-662-49924-5.
(23) Sleight, A.; Brixner, L. A new ferroelastic transition in some $A_2(MO_4)_3$ molybdates and tungstates. *J. Solid State Chem.* **1973**, *7*, 172−174.
(24) Jacques, S. D. M.; Leynaud, O.; Strusevich, D.; Beale, A. M.; Sankar, G.; Martin, C. M.; Barnes, P. Redox Behavior of Fe-Mo-O Catalysts Studied by Ultrarapid In Situ Diffraction. *Angew. Chem., Int. Ed.* **2006**, *45*, 445−448.
(25) Massarotti, V.; Flor, G.; Marini, A. Crystal data for ferric molybdate: $Fe_2(MoO_4)_3$. *J. Appl. Crystallogr.* **1981**, *14*, 64−65.
(26) Rapposch, M.; Anderson, J.; Kostiner, E. Crystal structure of ferric molybdate, $Fe_2(MoO_4)_3$. *Inorg. Chem.* **1980**, *19*, 3531−3539.
(27) Jirak, Z.; Salmon, R.; Fournes, L.; Menil, F.; Hagenmüller, P. Magnetic and Moessbauer resonance investigations of the weak ferrimagnet iron molybdate ($Fe_2(MoO_4)_3$). *Inorg. Chem.* **1982**, *21*, 4218−4223.
(28) Morin, F. J. Magnetic Susceptibility of αFe_2O_3 and αFe_2O_3 with Added Titanium. *Phys. Rev.* **1950**, *78*, 819−820.
(29) Battle, P. D.; Cheetham, A. K.; Long, G. J.; Longworth, G. Study of the magnetic properties of iron(III) molybdate, by susceptibility, Moessbauer, and neutron diffraction techniques. *Inorg. Chem.* **1982**, *21*, 4223−4228.
(30) Maksimov, Y.; Suzdalev, J.; Engelmann, H.; Gonser, U. Structural and magnetic properties of amorphous ferric molybdate compared to crystalline ferric molybdate. *Hyperfine Interact.* **1986**, *27*, 429−432.
(31) Orlandi, P.; Magistris, A.; Rigamonti, A. Mössbauer and Conductivity Study of Ferroelastic Ferric Molybdate. *Phys. Status Solidi A* **1982**, *72*, 543−549.